ACS central science

http://pubs.acs.org/journal/acscii

Outlook

Photovoltaic Energy Conversion and Storage of Micro-Supercapacitors Based on Emulsion Self-Assembly of Upconverting Nanoparticles

Wenna Wu, Jin Yuan, Shuli Dong, and Jingcheng Hao*

Cite This: *ACS Cent. Sci.* 2021, 7, 1611−1621

Read Online

ACCESS | Metrics & More | Article Recommendations | Supporting Information

ABSTRACT: With the rapid need for new kinds of portable and wearable electronics, we must look to develop flexible, small-volume, and high-performance supercapacitors that can be easily produced and stored in a sustainable way. An integrated system simultaneously converting recyclable energy to electricity and storing energy is sought after. Here we report photovoltaic energy conversion and storage integrated micro-supercapacitors (MSCs) with asymmetric, flexible, and all-solid-state performances constructed from thousands of close-packed upconverting nanoparticles (UCNPs) via an emulsion-based self-assembly process using oleic acid (OA)-capped upconverting nanoparticles. The carbonated-UCNPs supraparticles (CSPs) are further coated with polypyrrole (PPy) to improve their electrochemical performance. Such a design can develop CSPs@PPy as electrode materials with high gravimetric capacitance, 308.6 F g^{-1} at 0.6 A g^{-1}. The fabricated MSCs exhibit excellent areal capacitance, C_s = 21.8 mF cm^{-2} at 0.36 A cm^{-2} and E = 0.00684 mWh cm^{-2}, and have superior flexibility and cycling ability. The MSC devices have a sensitive near-infrared ray (NIR) photoelectrical response capability, which can capture the NIR of sunlight to convert it into electrical energy and store the electric energy due to an excellent capacitive performance. We propose a method for multifunctional integration of energy conversion and storage, and provide future research directions and potential applications of self-powered flexible wearable photonic electronics.

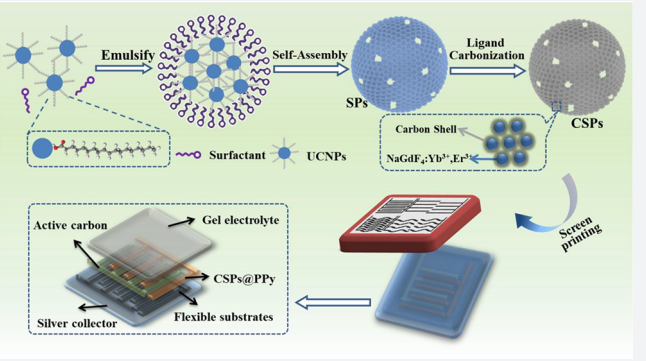

INTRODUCTION

In recent years, with the increasing demand for energy, it is essential to develop high-power, flexible, portable, lightweight, and reliable energy conversion and storage devices.[1−5] A complete energy system should integrate energy conversion and energy storage into one device,[6,7] and some types of energy conversion devices containing nanogenerators,[8] thermoelectric devices,[9] fuel cells,[5] and solar cells[10] have been widely developed. Among these, solar photovoltaic conversion technology, i.e., from light to electric energy, is an important way to realize green and renewable energy power generation. However, one of the limitations of solar cells is the low efficiency of photoelectric conversion. It is insensitive to the whole solar spectrum (280−2500 nm), and the light with a wavelength greater than 780 nm cannot be effectively absorbed.[11] One effective strategy is to use upconversion luminescent materials as a spectrum of a converter to expand the response range to the near-infrared region, improving the photoelectric conversion efficiency.[11,12] Meanwhile, electric energy generated from these renewable sources must be efficiently stored to meet energy demands. Supercapacitors (SCs) are considered as a promising electrochemical energy storage device, which are characterized by excellent power density, fast charge/discharge capacity at large currents, and long cycling life.[13−15]

Compared with traditional sandwiched SCs, the planar micro-supercapacitors (MSCs) with two interdigital electrodes have drawn much attention because of their light weight, small size, outstanding rate performance, and easy integration with other microdevices.[16,17] However, the practical applications of MSCs suffer the severe shortcomings of their low energy density (0.22 μWh cm^{-2}) and intricate fabrication process.[18] In order to further elevate the energy density ($E = (C \times \Delta V^2)/2$, where E is the energy density, C is the specific capacitance, and ΔV is the voltage window) of MSCs, asymmetric structure design and high-performance electrode materials can be introduced.[13]

The design of asymmetric structures for MSCs is an effective approach to elevate the energy density. Compared with

Received: July 3, 2021
Published: September 14, 2021

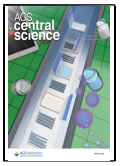

Scheme 1. (a) Preparation of UCNPs Superparticles and (b) Fabrication Process of MSCs with Structural Design

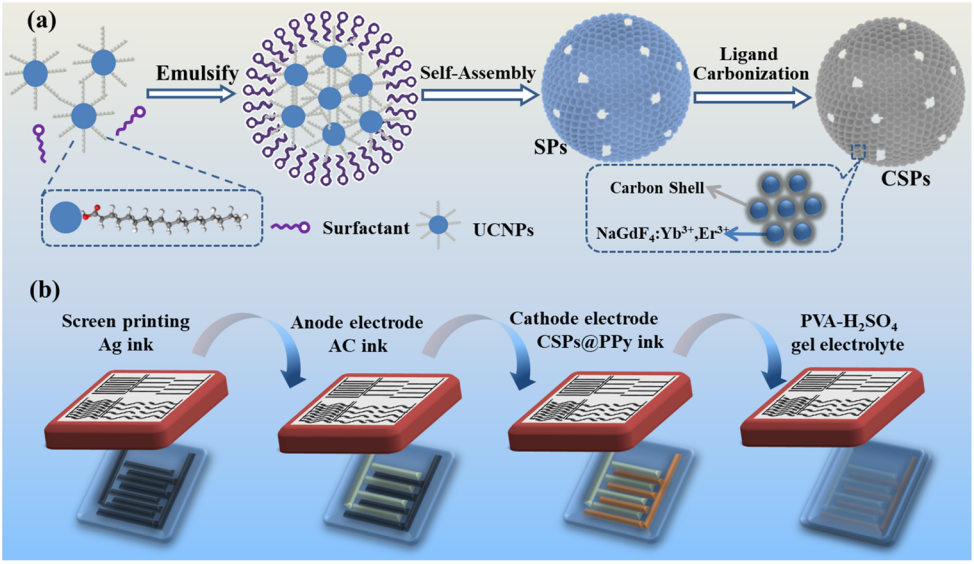

symmetric structure, an asymmetric design can broaden the voltage window of MSCs via utilizing two different work electrodes.[13] The asymmetric MSCs can be easily fabricated via a simple screen printing technique avoiding the high costs and lack of substrates of other techniques, including electrochemical depositing, laser scribing and plotter cutting, etc.[19] By screen printing, not only can the functional pattern of cathode and anode be accurately controlled, but also various flexible substrates can be chosen. Flexible MSCs with asymmetric electrode structures can be easily realized via a full screen printing process. The combination of high-performance electrode materials with an asymmetric structure design is an effective method to improve energy density. Apart from the asymmetric structural design, the selection of high-performance electrode materials is vital because it is the core component of MSCs. Various electrode materials such as carbon materials, metal oxides, and conductive polymer and hybrid materials have been extensively developed.[5,13,20] There is still a lack of an ideal model system to study the structure−activity relationship of electrode materials.

Colloidal nanocrystal superlattices are regarded as a new kind of condensed matter with a low-dimensional periodic array structure, which could be an ideal model system for electrode materials.[21] There are long-chain organic ligands such as oleic acid (OA) on the surface of colloidal nanoparticles (NPs), and these organic ligands may obstruct the transfer of charges, resulting in poor electrical conductivity. The traditional superlattices constructed by colloidal nanocrystals usually have a three-dimensional dense stacking structure, which restricts the mass transfer and thus hinders their applications. In order to solve these two problems, Dong et al. proposed a strategy of *in situ* ligand carbonization, where the nonconductive long-chain organic ligands are carbonized into an ultrathin conductive carbon-coating layer by *in situ* heat treatment, enhancing the conductivity without additional carbon precursors for forming NPs/carbon composites.[22,23] Compared with traditional colloidal NPs such as Fe_3O_4, upconversion nanoparticles (UCNPs) are promising candidates as electrode materials for MSCs on account of their superior conductivity and photovoltaic property.[11] Lanthanide-doped upconversion luminescent materials with multiple 4f electronic energy states can absorb near-infrared (NIR) light and emit visible light, exhibiting extensive applications from bioimaging to photovoltaic technologies.[24] Recent research on upconversion materials mainly focuses on the luminescent property, while the excellent photovoltaic property acting as electrode materials has not been thoroughly explored. As a kind of photovoltaic material, UCNPs capped with OA ligands are supposed to be promising building blocks to fabricate MSCs by self-assembling into hollow superlattice assemblies. This device is expected to integrate energy harvesting (absorbing the NIR light with a wavelength greater than 780 nm) and energy storing on one plane with a small volume.

In this outlook, we present asymmetric, flexible, and all-solid-state MSCs resulting from self-assembly of hollow supraparticles composed of thousands of close-packed UCNPs with superior conductivity and photovoltaic property. The whole system is achieved by continuously screen printing a silver current collector, activated carbon (AC) inks (anode electrode), CSPs@PPy (cathode electrode), and gel electrolyte onto PET flexible substrates as shown in Scheme 1. Our UCNPs supraparticles (SPs) with hollow interiors and hierarchical porous structure are successfully obtained by an emulsion-based self-assembly process using OA-capped UCNPs. The hollow porous structures and photovoltaic property are integrally retained during the ligand carbonization process, where the close-packed carbon shells derived from the native OA ligands *in situ* generate an interconnected electron transport network, enhancing the electrochemical activity. To further improve the electrochemical performance, a polypyrrole (PPy) conductive polymer is coated on the surface of the CSPs through electrostatic interaction. Such a design can develop CSPs@PPy as electrode materials with a high gravimetric capacitance, 308.6 F g^{-1} at 0.6 A g^{-1}. The fabricated MSCs possess high areal capacitance, C_s = 21.8 mF cm^{-2} at 0.36 A cm^{-2} and E = 0.00684 mWh cm^{-2}, superior flexibility, outstanding cycling ability, and sensitive NIR photoelectrical response. These MSCs based on UCNP-SPs are expected to be developed toward multifunctional integration, energy conversion, and energy storage in flexible wearable electronics.

https://doi.org/10.1021/acscentsci.1c00795
ACS Cent. Sci. 2021, 7, 1611−1621

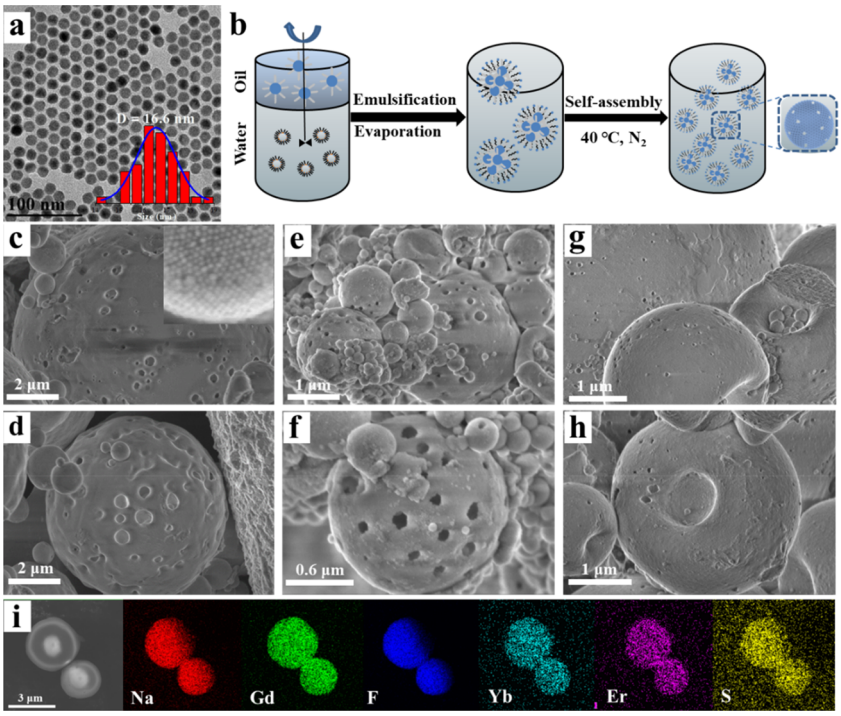

Figure 1. (a) TEM image of the OA-stabilized lanthanide-doped upconversion nanoparticles, $NaGdF_4$: Yb^{3+}, Er^{3+}; inset is the size distribution of UCNPs. (b) Schematic illustration of the stepwise assembly process. (c, d) SEM images of UCNPs-SPs at c_{SDS} = 200 mg mL^{-1}, (e, f) at the concentration of perfluorinated sodium octanoate, 10 mg mL^{-1}, (g, h) at the concentration of sodium heptadecafluorobenzenesulfonate, 10 mg mL^{-1}. (i) Elemental mapping of SPs formed with SDS.

RESULTS AND DISCUSSION

UCNPs and Hollow Supraparticles Assemblies. The OA-stabilized lanthanide-doped upconversion nanoparticles, $NaGdF_4$: 20% Yb^{3+}, 2% Er^{3+} were synthesized by a thermal decomposition method with modification of our previous works.[24−26] The TEM image of the UCNPs in Figure 1a suggests that the nanoparticles are uniform and have an average diameter of about 16.6 nm determined by random measurement of 100 particles. These prepared UCNPs are used as building blocks to fabricate assemblies of SPs based on a surfactant-assisted emulsion self-assembly method. Figure 1b illustrates the stepwise assembly process, in which the hydrophobic UCNPs are confined in the oil droplets stabilized by surfactants, while the subsequent hexane evaporation forces the NPs to pack densely within the emulsion droplets. The effect of different types of surfactants on the solid/hollow structure of SPs is primarily explored. According to the classification of surfactants, there are ionic, nonionic, natural, and novel surfactants to be explored successively.

When cationic and nonionic surfactants were respectively used as an emulsifier to perform the emulsion self-assembly, no ordered SPs were generated; only monodisperse small-sized UCNPs were observed by TEM in Figure S1 in the Supporting Information. The amphoteric surfactant was explored, and it was found that in Figure S2 in the Supporting Information when the pH is lower than the isoelectric point of the surfactant, no assembly appears (Figure S2b in the Supporting Information), while the assembly forms when the pH is higher than the isoelectric point (Figure S2c in the Supporting Information). It is supposed that the electrostatic repulsion between surfactants and UCNPs may hinder the formation of SPs, which is consistent with our previously reported results.[26] Our attention is focused on different types of anionic surfactants. The names and chemical structures of anionic surfactants are summarized in Table S1 in the Supporting Information. From TEM and SEM images shown in Table S1 in the Supporting Information, one can see the thin-walled hollow capsules formed with the concentration of bioactive surfactant sodium deoxycholate increasing to 30 mg mL^{-1}. The other types of anionic surfactants with various concentrations in Table S1 in the Supporting Information all can drive UCNPs assembly to form solid SPs, as shown in the TEM and SEM images.

For anionic SDS, two factors are found to dramatically affect the architecture of UCNPs-SPs. One is the SDS concentration, and the other is the temperature. With the increase of SDS concentration from 100 to 200 mg mL^{-1} at fixed other parameters, the large UCNPs-SPs with holes on the surface appear, suggesting their hollow interiors, as shown in Figure 1c,d, which may be caused by the concentration control factors. The reason may be that with the concentration of SDS increasing to 200 mg mL^{-1}, the surface tension of the emulsion droplets decreases. It results in the outward diffusion force greater than that of the inward compression force, which is conducive to the formation of a hollow and porous structure.[27] Similarly, the surfactants of perfluorinated sodium octanoate (Figure 1e,f) and sodium heptadeca-fluorobenzenesulfonate (Figure 1g,h) can also lead to UCNPs-SPs with hollow and porous structures at low surfactants concentration, c = 10 mg mL^{-1}; it should be attributed to the high surface activity of perfluorinated surfactants.

Temperature may control the formation of porous and hollow structures. When the evaporation temperature is controlled to be 40 °C, the outward diffusion force is enlarged, which is favorable for UCNPs to move toward the surface of droplet and increases the possibility of forming hollow

https://doi.org/10.1021/acscentsci.1c00795
ACS Cent. Sci. 2021, 7, 1611−1621

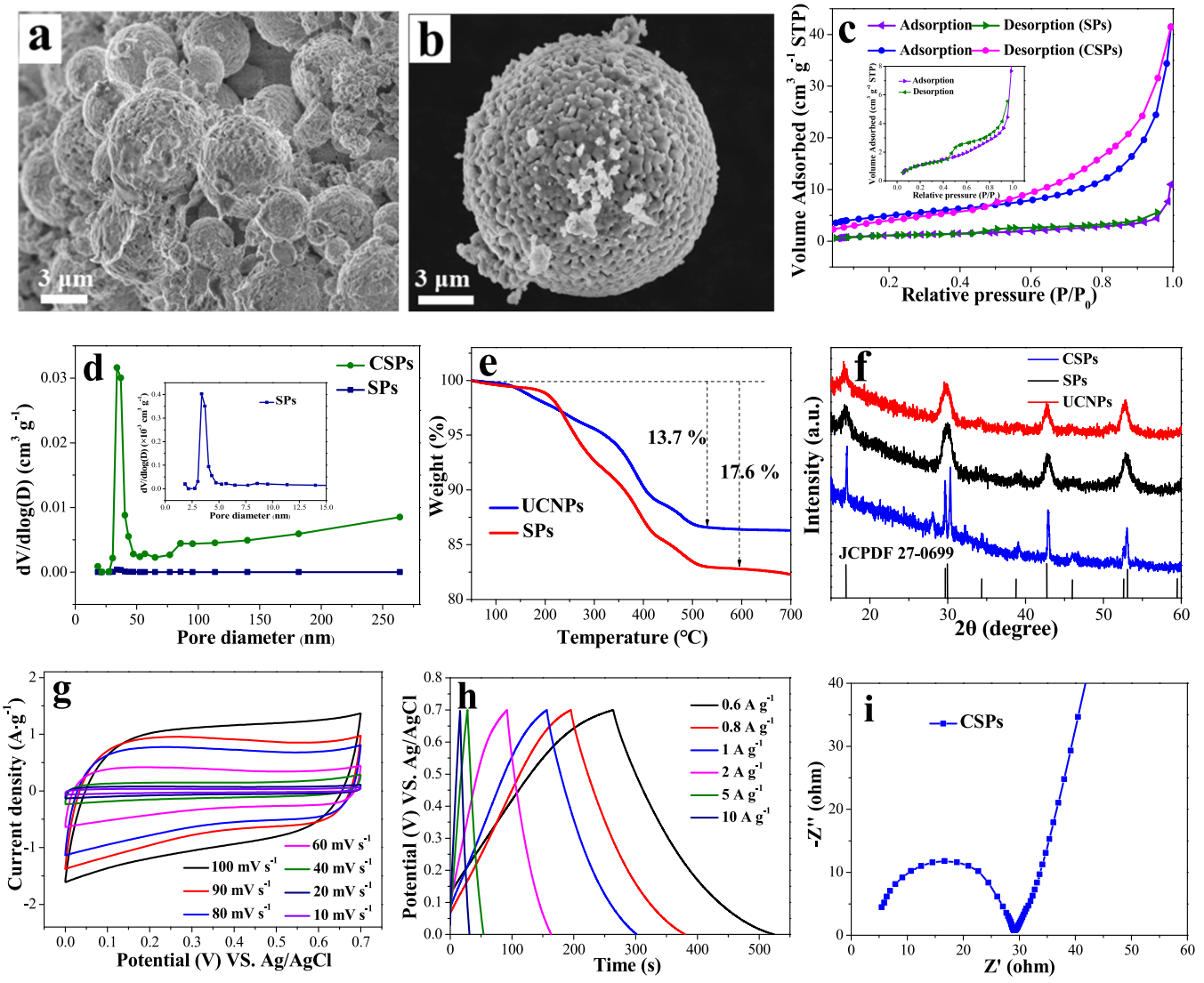

Figure 2. (a and b) SEM images of CSPs. (c) N_2 adsorption−desorption isotherms, inset is the enlarged curve of SPs. (d) Pore width distribution of SPs and CSPs, inset is the enlarged curve of SPs. (e) TGA curves of UCNPs and SPs. (f) XRD patterns of UCNPs, SPs, and CSPs. (g) CV curves of the CSPs electrode at different scan rates. (h) GCD curves of the CSPs electrode at different current densities. (i) Nyquist plot of the CSPs electrode.

structures.[28] At T = 40 °C, it is helpful to the formation of a dynamically stable hollow structure.[29] The SEM images in Figure 1c−h show hollow and porous UCNPs-SPs composed of thousands of densely packed UCNPs. The diameter of SPs ranges from 200 nm to 5 μm, which is smaller than that of the corresponding emulsion droplet in Figure S3 in the Supporting Information, indicating that the shrinkage of the emulsion droplet is accompanied by the inner solvent volatilization. Elemental mapping of single SPs formed with SDS reveals the homogeneous distribution of UCNPs and SDS (Figure 1i).

CSPs and Electrochemical Performance. To improve the comprehensive performance of SPs-based supercapacitors, it is necessary to optimize the electrical conductivity. Carbonization of the organic OA ligands around the UCNPs is a good way. The assembled UCNPs-SPs were heated at 500 °C under argon protection to carbonize the OA ligands, converting the organic ligands into a thin carbon layer without changing the ordered superlattices structure of UCNPs, as demonstrated by SEM images in Figure 2a,b. After the ligand carbonization, the hollow structure of CSPs retains its structural integrity without collapse, suggesting that the neighboring carbon coating is interconnected with each other to afford 3D continuous carbon networks. This hypothesis can be corroborated by N_2 adsorption−desorption measurements and XRD characterizations.

As shown in Figure 2c, both of the SPs and CSPs exhibit type-IV isotherms with a Brunauer−Emmett−Teller (BET) specific surface area, 4.4 $m^2 g^{-1}$ and 17.8 $m^2 g^{-1}$, respectively. The large hysteresis loops can be observed at P/P_0 of 0.47, indicating the existence of mesoporous structures in the materials, in agreement with SEM observations. The pore diameter is enlarged from 3.4 to 35.2 nm after the ligand carbonization, as shown in the BJH pore width distribution curve (Figure 2d). One can see that the carbonization leads to an increase of the specific surface area and pore diameter, suggesting again that the interiorly or superficially obtained carbon coating affords CSPs with 3D continuous carbon networks. Elemental mapping of CSPs reveals the homogeneous distribution of carbon (Figure S4 in the Supporting Information), further indicating the existence of 3D con-

https://doi.org/10.1021/acscentsci.1c00795
ACS Cent. Sci. 2021, 7, 1611−1621

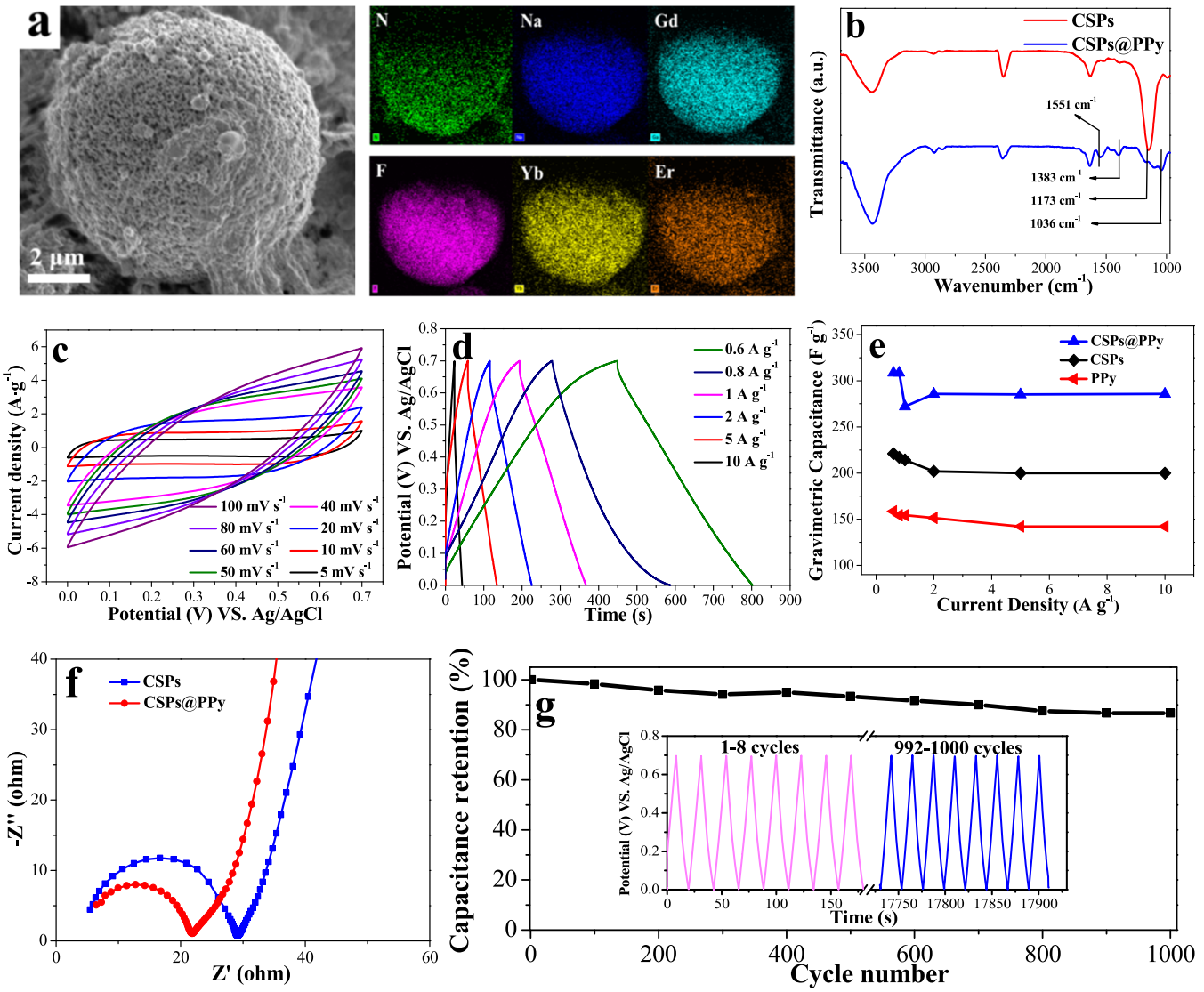

Figure 3. (a) SEM image and elemental mapping of CSPs@PPy. (b) FT-IR spectra of CSPs and CSPs@PPy. (c) CV curves of CSPs@PPy electrode at different scan rates. (d) GCD curves of CSPs@PPy electrode at different current densities. (e) Gravimetric capacitances (C_m) of PPy, CSPs, and CSPs@PPy electrodes at different current densities. (f) Nyquist plots of CSPs and CSPs@PPy electrode. (g) Cyclic stability of CSPs@PPy electrode; inset is several GCD curves (1−8 and 992−1000) during the electrochemical cycles.

tinuous carbon networks after ligand carbonization. The UCNPs in CSPs shell are independent and cross-linked to each other through carbon-coated networks to form interconnected electron transport networks, enabling the UCNPs electrochemical activity. A TGA test in N_2 is employed to determine the carbon content of SPs. According to the weight loss data of the TGA curves in Figure 2e, the carbon content is 13.7 and 17.6 wt % for UCNPs and SPs, respectively, indicating that the content of the surfactant in SPs assembly is 3.9%. The increase of carbon content could be conducive to improving the conductivity. The XRD characterization in Figure 2f confirms that both SPs and CSPs exhibit the characteristic peaks of the hexagonal phase $NaGdF_4$, indicating that the process of ligand carbonization does not change the crystal phase of UCNPs, which can maintain the excellent photovoltaic property.

To study the electrochemical performance of the CSPs as anode, cyclic voltammetry (CV), galvanostatic discharge−charge (GCD), and electrochemical impedance spectrum (EIS) measurements are performed via a three-electrode system in a liquid electrolyte of 0.1 M aqueous KCl solution. The CV curves of CSPs electrode with different scan rates from 10 to 100 mV s^{-1} are presented in Figure 2g. The curves are all quasi-rectangular shape in the voltage range of 0−0.7 V, indicating the excellent capacitance performance. Figure 2h shows the GCD curves at different current densities from 0.6 to 10 A g^{-1} with an almost symmetrical triangular peak, which is consistent with the CV curves and implies the characteristics of good double-layer capacitance. Figure 2i records the Nyquist plot of CSPs electrode at 100 kHz to 0.1 Hz by EIS measurements. A traditional semicircle electrochemical capacitor behavior is observed, which is related to the charge transfer resistance (R_{ct}) and equivalent resistance (R_c). The small semicircle of the CSPs electrode demonstrates a good conductivity, which is beneficial to the capacitance behavior. All of the above tests show that the CSPs can serve as an ideal electrode material for supercapacitors.

CSPs@PPy and Electrochemical Performance. To further improve the electrochemical performance, the CSPs are enveloped with a conductive PPy shell to form CSPs@PPy.

https://doi.org/10.1021/acscentsci.1c00795
ACS Cent. Sci. 2021, 7, 1611−1621

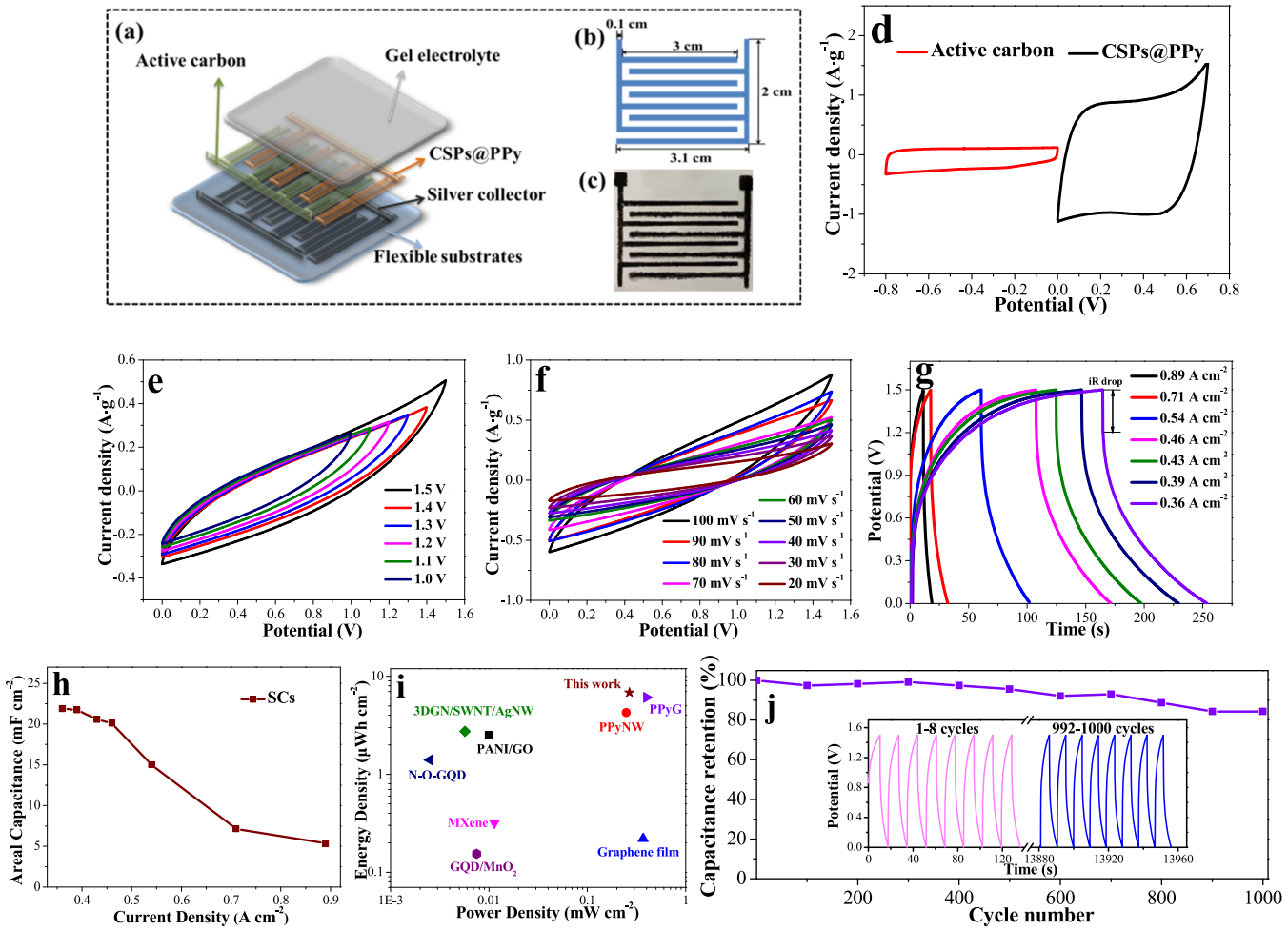

Figure 4. (a) Structural design of asymmetric MSCs. (b) The dimension of screen printing patterns. (c) The devices of asymmetric, flexible, and all solid-state MSCs based on a PET flexible substrate. (d) Capacity match of the CSPs@PPy positive electrodes and AC negative electrodes. CV curves of the asymmetric MSCs device (e) with different voltage windows at a scan rate of 60 mV s^{-1} and the (f) fixed windows at different scan rates (20−100 mV s^{-1}). (g) GCD curves of MSC devices at different current densities (0.36−0.89 A cm^{-2}). (h) Areal capacitances (C_s) of MSCs calculated from GCD curves at different current densities (0.36−0.89 A cm^{-2}). (i) Ragone plot of the CSPs@PPy MSCs compared with other previous MSCs. (j) Cyclic stability of MSC the device; inset is several GCD curves (1−8 and 992−1000) during the electrochemical cycles.

The pyrrole with positive charges greatly tends to adsorb on the surface of negatively charged CSPs (originating from SDS-capped SPs, as shown in Figure S5) through electrostatic attraction. After oxidation polymerization, the pyrrole monomers can directly polymerize on the CSPs surface to form a uniform PPy layer. The SEM images in Figure 3a demonstrate a clear porous structure of CSPs@PPy, and the elemental mapping of CSPs@PPy shows the homogeneous distribution of nitrogen (Figure 3a), indicating the successful preparation of CSPs@PPy. As shown in FT-IR spectra (Figure 3b), the peaks of CSPs@PPy at 1551, 1383, 1173, and 1036 cm^{-1} represent C═C vibration, C−C stretching vibration, C−N stretching vibration, and C−H in-plane bending vibration of PPy, respectively. In Figure S5, zeta potential data provide further evidence of the successful PPy coating on the surface of CSPs, where the changes of zeta potential are from CSPs with −49.4 mV to CSPs@PPy with 4.8 mV.

We tested the electrochemical properties of the CSPs@PPy electrode. As shown in Figure 3c, CV plots of the CSPs@PPy electrode at different scan rates ranging from 10 to 100 mV s^{-1} at a working potential window of 0−0.7 V are carried out. All curves display the symmetrical slant rectangular shape, and even the scan rate reaches 100 mV s^{-1}, indicating that the CSPs@PPy electrode possesses the ideal capacitance behavior and can work stably within 0−0.7 V. Corresponding to CV tests, the GCD curves of the CSPs@PPy electrode in Figure 3d show a relative symmetric triangle at different current densities (0.6−10 A g^{-1}), suggesting the characteristics of double-layer capacitance. The CV and GCD curves of pure PPy electrode are also measured in the same case as shown in Figure S6 in the Supporting Information in order to evaluate the contribution of PPy to the capacitance of the CSPs@PPy composite. The gravimetric capacitances (C_m) of all electrodes are calculated from the GCD curves according to following equation:

$$C_m = \frac{I\Delta t}{m\Delta V} \tag{1}$$

where C_m is gravimetric capacitances (F g^{-1}), I is discharge current (A), Δt is discharge time (s), m is the mass of active substance (g), ΔV is the operating potential window (V). Figure 3e shows the calculated results of gravimetric capacitances, where the PPy electrode, CSPs electrode, and CSPs@PPy electrode are 158.6, 221.1, and 308.6 F g^{-1} at a

https://doi.org/10.1021/acscentsci.1c00795
ACS Cent. Sci. 2021, 7, 1611−1621

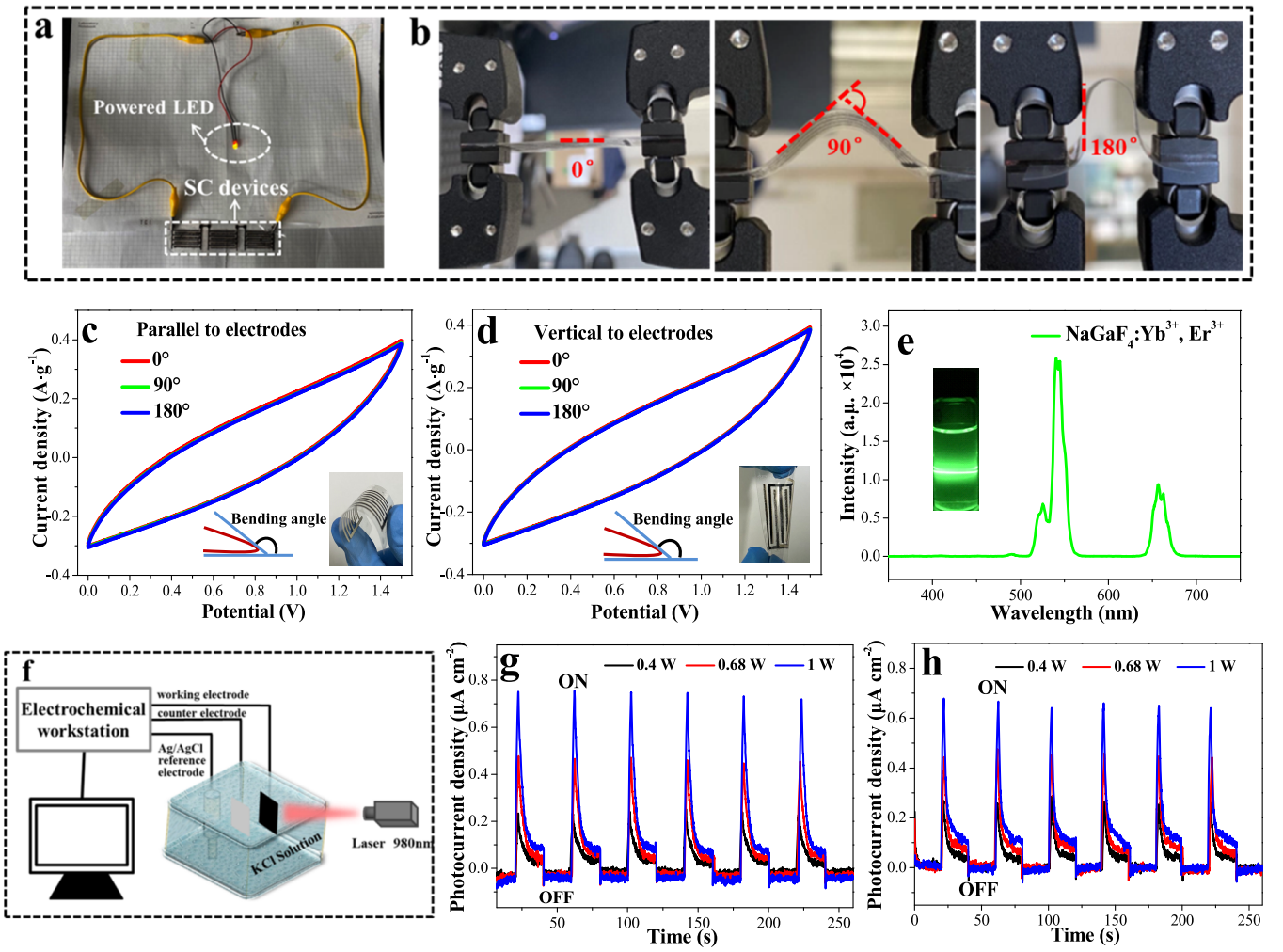

Figure 5. (a) Photographs of a red LED powered by charged MSCs. (b) Schematic diagram of different bending angles for MSCs. (c) CV curves of MSCs for different bending angles (0°, 90°, and 180°) at the direction parallel to electrodes and (d) vertical to electrodes. (e) UC emission spectra of UCNPs; inset is the image of UCNPs dispersed in hexane with excitation of 980 nm laser. (f) Schematic diagram of the photoelectric response system. (g) The curves of the photocurrent response of UCNPs. (h) CSPs@PPy, where the light source is toggled every 20 s.

current density of 0.6 A g^{-1}, respectively. Obviously, the CSPs@PPy electrode possesses the highest gravimetric capacitances at every current density, indicating the great capacitance performance enhancement through the composite method. The C_m can remain about 90% as high as 280 F g^{-1}, while the current density increases to 10 A g^{-1}. The excellent capacitance performance of CSPs@PPy might be attributed to the enhancement of conductivity from PPy. EIS tests of the CSPs electrode and CSPs@PPy electrodes are displayed in Figure 3f; the semicircle diameter of CSPs@PPy electrodes is smaller than that of CSPs electrode in Nyquist plots, demonstrating the charge transfer resistance is decreased and the conductivity is increased by the introduction of PPy. The cycling stability tests of CSPs@PPy electrodes are presented in Figure 3g. After 1000 continual cycles of GCD tests at a current density of 0.6 A g^{-1}, the CSPs@PPy electrode can retain 85% of the original capacitance, displaying an excellent electrochemical stability of the CSPs@PPy composite.

Electrochemical Performance of Asymmetric MSCs. We fabricated the asymmetric MSCs by a fully screen printing technique illustrated in Scheme 1b. The structural design of asymmetric MSCs is shown in Figure 4a, with PET film as substrates, conductive silver as the current collector, CSPs@PPy as the cathode, AC as the anode, and PVA/H_2SO_4 as the gel electrolyte coating onto electrode materials forming a quasi-solid-state planar device. The dimension and finger width of screen printing patterns are presented in Figure 4b. According to different requirements, we design the different patterns of the asymmetric MSCs, such as finger fork and wave fork in Figure S7a in the Supporting Information. Flexible substrates such as PET and A4 paper are available. Connecting three MSCs devices in series is designed to improve the overall voltage window in Figure S7b in the Supporting Information. The resulting asymmetric, flexible, and all solid-state MSCs device based on PET flexible substrates are displayed in Figure 4c. The capacity match between CSPs@PPy positive (0−0.8 V) and AC negative (−0.7−0 V) electrodes is shown in Figure 4d, indicating the ability of approximate energy storage. As presented in Figure 4e, the MSCs device can realize the maximum voltage window of 1.5 V due to the asymmetric design. The device exhibits nearly rectangular CV curves at various scan rates from 20 to 100 mV s^{-1} within an operating potential window of 0−1.5 V in Figure 4f, indicating the excellent capacitive behavior of the fabricated MSCs. GCD curves of the MSC device at various current densities in a broad operating voltage window of 0−1.5 V with a nearly

https://doi.org/10.1021/acscentsci.1c00795
ACS Cent. Sci. 2021, 7, 1611−1621

symmetric triangle in Figure 4g also demonstrate the great capacitive performance. However, comparing with the curves of CSPs@PPy as shown in Figure 3c and Figure 3d, the MSCs device presents a slightly distortion, which may indicate a larger equivalent series resistance (ESR), resulting from bridge connections with conductive silver current collector.[30] The areal capacitance (C_s), energy density (E_s), and power density (P_s) are calculated according to following equations:[31]

$$C_s = \frac{I\Delta t}{S\Delta V} \tag{2}$$

$$E_s = \frac{1}{2 \times 3600} \times C_s \times (\Delta V)^2 \tag{3}$$

$$P_s = \frac{E_s}{\Delta t} \tag{4}$$

where I is the discharge current (A), Δt is the discharge time (s), S is the electrode area (m^2), and ΔV is the operating potential window (V). The results of C_s of MSCs calculated from GCD curves are indicated in Figure 4h. It can be seen that, at a current density of 0.36 A cm^{-2}, the C_s of the MSCs can reach 21.8 mF cm^{-2}, confirming the MSCs has an ideal capacitance. At a current density of 0.36 A cm^{-2}, a large P_s of 0.268 mW cm^{-2} can be achieved at an E_s of 0.00684 mWh cm^{-2}. To evaluate our CSPs@PPy-based MSCs, a summary of the electrochemical performance of the MSCs in previous published works including different types of active materials is listed in Table S2 in the Supporting Information and the comparison is displayed in a Ragone plot (Figure 4i).[18,19,32,33] Obviously, our CSPs@PPy-based MSCs present higher energy and power densities than most of the reported MSCs, demonstrating excellent power capability of as-fabricated MSCs.

Apart from the high energy density and superior power capability, the electrochemical stability is another pivotal factor that should be noticed for an applied supercapacitor. The electrochemical cycling stability of the MSCs is measured during a cyclic charge/discharge process at a current density of 0.36 A cm^{-2} in Figure 4j. It can be seen that, after 1000 continual cycles of GCD tests, the MSCs devices can retain 83% of the original capacitance, indicating the excellent electrochemical stability of MSCs devices. The practical application of the MSCs devices is explored, in which we connect three MSCs devices in series as shown in Figure 5a, where a commercial red LED (2 V) could be successfully lit after the MSC devices are charged by electrochemical workstation, suggesting that the fabricated flexible all-solid-state MSCs have practical application in energy storage. The planar and flexible MSC device possesses great mechanical flexibility and stability, which is confirmed by the bending test in Figure 5b. The effect of the bending angle (0°, 90°, and 180°) and bending direction (parallel or vertical to electrodes) on the capacitance performance is shown in Figure 5c,d, in which the CV curves almost completely overlap when bending at different angles parallel or vertical to the electrode, respectively. This indicates that the flexible MSCs device presents outstanding mechanical flexibility and stability, implying the great potential in storage energy for portable or flexible electronics.

Photovoltaic Property of UCNPs and MSCs Devices. The term "upconversion" describes an optical process of nonlinear anti-Stokes that convert two (or more) low-energy pump photons to a higher-energy output photon.[34] Acting as luminescent materials, UCNPs could convert a broad spectrum of light into photons of a particular wavelength. To demonstrate the potential application of UCNPs in NIR photoelectric devices, we measured the UC emission spectra. As shown in Figure 5e, the UCNPs exhibit obvious green emission peaks under a laser excitation of 980 nm. The peaks at 525, 540, and 656 nm can be attributed to the transitions of Er^{3+}: $^2H_{11/2} \rightarrow {}^4I_{15/2}$, $^4S_{3/2} \rightarrow {}^4I_{15/2}$, and $^4F_{9/2} \rightarrow {}^4I_{15/2}$, respectively. As has been reported, only when the energy absorbed by the photons is higher than the bandgap can electron−hole pairs be generated, which contributes to generate the electric current.[11] The transmission of sub-bandgap photons is one of the major energy loss mechanisms in the process of energy conversion, especially for conventional solar cells. Photon upconversion supplies an effective method to avoid this transmission loss by converting unutilized sub-bandgap NIR photons into useful bandgap visible photons.[35,36]

To investigate the photoelectric effect of UCNPs under the exposure of NIR 980 nm, the schematic diagram of the photoelectric response system is shown in Figure 5f. The photocurrent response of UCNPs is recorded by $I-T$ curves using an electrochemical workstation, where the light source is toggled every 20 s. Notably, UCNPs exhibit an obvious photoelectric effect under the 980 nm excitation as shown in Figure 5g. The MSCs devices also generate a photocurrent when the MSCs are irradiated by a 980 nm laser in Figure 5h. The NIR photoelectric response of UCNPs is a combined effect of upconversion and energy transfer. This inner photoelectric effect is mainly dependent on the absorption cross-section in the NIR area of the Er^{3+}.[37] When the samples are illuminated by a 980 nm laser, two paratactic processes occurred. The first one is that a part of absorbed NIR light with low energy by UCNPs is translated into shorter-wavelength visible light with high energy, leading to the UC luminescence (Figure 5f). The other one is that absorbed NIR light stimulates the electrons of UCNPs to transfer from the valence band (VB) to the conduction band (CB) via the UC pathway, resulting in the generation of many free electrons in the sample and presenting a NIR photoelectric effect, as shown in Figure 5g,h. As we can see, the response photocurrent of UCNPs and MSCs devices increases with the elevation of laser power ranging from 0.4 to 1 W, respectively. After UCNPs is assembled into MSCs devices, there is no significant difference in the photocurrent performance under the same light source power as shown in Figure 5h, indicating that the assembly could not affect the photoelectric conversion performance.

In this system, the CSPs@PPy based on UCNPs is selected as the electrode material, which shows excellent electrochemical properties and photovoltaic conversion properties. The asymmetric, flexible, and all solid-state MSCs based on CSPs@PPy may be designed into an integrated device, which could capture the NIR light of solar light and convert it into electric energy, and this electric energy can be efficiently stored due to excellent capacitive performance of the MSC device. The function of energy conversion and storage in CSPs@PPy materials-based MSCs will be a good substitute for green and renewable energy.

CONCLUSIONS

To conclude, asymmetric, flexible, and all solid-state MSCs composed of hollow UCNPs supraparticles have been successfully fabricated by a screen printing technique. The

https://doi.org/10.1021/acscentsci.1c00795
ACS Cent. Sci. 2021, 7, 1611−1621

UCNPs supraparticles with hollow interiors and a hierarchical porous structure excite superior conductivity and photovoltaic properties. Under ligand carbonization, the hollow porous structures and photovoltaic properties of CSPs are integrally retained, and the generated close-packed carbon shells derived from the native OA ligands provide an interconnected electron transport network enhancing the electrochemical activity. The synthesis of CSPs@PPy improves the electrochemical performance. The functional layers are directly printed onto flexible PET substrates to construct MSCs in the order of silver current collector, cathode electrode, anode electrode, and gel electrolyte. The fabricated MSCs exhibited excellent areal capacitance, C_s = 21.8 mF cm^{-2} at 0.36 A cm^{-2} and E = 0.00684 mWh cm^{-2}, superior flexibility, and outstanding cycling ability. The MSCs devices can capture the NIR light of solar light and convert into electric energy because of the ability of the sensitive NIR photoelectrical response, and the electric energies could be efficiently stored due to excellent capacitive performance. We suppose that the screen printed flexible all-solid-state MSCs can be a promising multifunctional integration device, i.e., energy conversion and energy storage for application in flexible wearable electronics in the future.

METHODS

Synthesis of $NaGdF_4$: Yb^{3+}, Er^{3+}. Lanthanide-doped UCNPs were synthesized following our previously reported procedures by a thermal decomposition.[24−26] For details, see the Supporting Information.

Emulsion-Based Self-Assembly of UCNPs and Synthesis of CSPs. Upconversion nanoparticles (UCNPs) and supraparticles (SPs) were obtained by an emulsion-based self-assembly process as reported previously.[26,27] Hexane solution of UCNPs was used as the oil phase, into which different types of surfactant aqueous solutions with various concentrations were added. Then the mixture was stirred and emulsified to form an oil-in-water emulsion system. After stabilization, the emulsion mixture was heated to 40 °C and kept for 8 h, in which with the organic solvent volatilizing hydrophobic forces drive the nanoparticles to self-assemble forming SPs. The hollow and porous structures of SPs were obtained by controlling different kinds of surfactants and different concentrations to regulate surface properties.

To be used as electrode materials, UCNPs-SPs were carbonized for 2 h at 500 °C under argon protection forming carbonated-supraparticles (CSPs), where the organic OA ligand of UCNPs and surfactant layers on the surface of SPs were carbonized into ultrathin conductive carbon layers.

Preparation of CSPs@PPy. To grow PPy layers onto the surface of CSPs, the conductive polymer PPy was first prepared. The ethanol solution (5 mL) containing 200 μL of pyrrole was added into HCl aqueous solution (1 M, 10 mL) under stirring for 30 min. Subsequently, 400 mg of ammonium persulfate dissolved in 10 mL of water was gradually added to trigger the polymerization of pyrrole with the color darkening. The obtained products were centrifuged and washed with ethanol/water for three times and then vacuum-dried at 60 °C. The CSPs@PPy was prepared similarly to PPy, except the needs of adding CSPs into HCl aqueous solution.

Formulation of CSPs@PPy and AC Printing Inks. The CSPs@PPy screen printing ink was prepared through dispersing 70 wt % CSPs@PPy active materials, 15 wt % conductive carbon black, and 15 wt % tackifier into DI water. Similarly, 70 wt % activated carbon, 15 wt % carbon black, and 15 wt % tackifier were dispersed into DI water forming AC screen printing ink.

Fabrication of Asymmetric, Flexible, and All-Solid-State MSCs by Screen Printing Technology. We used a simple and efficient technique of screen printing to fabricate the MSCs in all steps, as shown in Scheme 1b. The functional inks could be briefly moved onto substrates through the screen to form designed patterns utilizing the screen printing technique, and the photographs of the designed printing plate and overall screen printing process are displayed in Figure S8 and Video S1, respectively. The detailed printing process is presented in Supporting Information.

Electrochemical Measurements. The electrochemical performances of the as-prepared CSPs@PPy material were tested through a three-electrode method. The working electrode was fabricated through depositing a 200 μL solution of CSPs@PPy onto the carbon cloth with a mass concentration of 5 mg mL^{-1} (CSPs@PPy dispersed in 1 mL of ethanol with 40 μL of Nafion). The electrochemical test was performed in 0.1 M KCl solution, and the platinum plate as the opposite electrode and Ag/AgCl as the reference electrode. The as-fabricated MSCs devices were tested in a two-electrode system with the prepared gel electrolyte.

Photoelectric Conversion Measurements. The photoelectric conversion property of CSPs@PPy was measured in a three-electrode system, and the diagram of a simple photocurrent testing device as shown in Figure 5e. The photocurrent was obtained by recording $I-T$ curves of CSPs@PPy under the irradiation of the 980 nm laser. The light source was turned off every 20 s, and the obtained current value was recorded.

Safety Statement. No unexpected or unusually high safety hazards were encountered.

ASSOCIATED CONTENT

Supporting Information

The Supporting Information is available free of charge at https://pubs.acs.org/doi/10.1021/acscentsci.1c00795.

Additional experimental procedures, TEM images, zeta potential, photographic images, size distribution of emulsion droplets, SEM elemental mapping, CV curves, patterns with different shapes and flexible substrates, photographs of designed printing plate (PDF)

Video of the overall screen printing process (MP4)

AUTHOR INFORMATION

Corresponding Author

Jingcheng Hao − *Key Laboratory of Colloid and Interface Chemistry, Ministry of Education and State Key Laboratory of Crystal Materials, Shandong University, Jinan 250100, P. R. China*; orcid.org/0000-0002-9760-9677; Phone: +86-531-88366074; Email: jhao@sdu.edu.cn

Authors

Wenna Wu − *Key Laboratory of Colloid and Interface Chemistry, Ministry of Education, Shandong University, Jinan 250100, P. R. China*

Jin Yuan − *Key Laboratory of Colloid and Interface Chemistry, Ministry of Education, Shandong University, Jinan 250100, P. R. China*

Shuli Dong − *Key Laboratory of Colloid and Interface Chemistry, Ministry of Education, Shandong University, Jinan 250100, P. R. China*; orcid.org/0000-0003-3961-7238

https://doi.org/10.1021/acscentsci.1c00795
ACS Cent. Sci. 2021, 7, 1611−1621

Complete contact information is available at:
https://pubs.acs.org/10.1021/acscentsci.1c00795

Notes

The authors declare no competing financial interest.

■ ACKNOWLEDGMENTS

J.H. gratefully acknowledges support of this work by the National Natural Science Foundation of China (Grant Nos. 22032003 and 22072073) and the Natural Science Foundation of Shandong Province (ZR2018ZA0547). We would like to acknowledge the technical support from Shandong University Structural Constituent and Physical Property Research Facilities.

■ REFERENCES

(1) Ribeyron, P. J. Crystalline silicon solar cells: Better Than Ever. *Nat. Energy* **2017**, *2*, 17067.
(2) Massiot, I.; Cattoni, A.; Collin, S. Progress and prospects for ultrathin solar cells. *Nat. Energy* **2020**, *5*, 959−972.
(3) Kyerematen, N. A.; Brousse, T.; Pech, D. Microsupercapacitors as miniaturized energy storage components for on-chip electronics. *Nat. Nanotechnol.* **2017**, *12*, 7−15.
(4) Dubal, D. P.; Chodankar, N. R.; Kim, D.-H.; Gomez-Romero, P. Towards flexible solid-state supercapacitors for smart and wearable electronics. *Chem. Soc. Rev.* **2018**, *47*, 2065−2129.
(5) Qiu, M.; Sun, P.; Cui, G.; Tong, Y.; Mai, W. A flexible microsupercapacitor with integral photocatalytic fuel cell for self-charging. *ACS Nano* **2019**, *13*, 8246−8255.
(6) Chai, Z.; Zhang, N.; Sun, P.; Huang, Y.; Zhao, C.; Fan, H.; Fan, X.; Mai, W. Tailorable and wearable textile devices for solar energy harvesting and simultaneous storage. *ACS Nano* **2016**, *10*, 9201−9207.
(7) Zhang, S.; Jiang, Q.; Wu, Z.; Ding, W.; Zhang, L.; Alshareef, H. N.; Wang, Z. Energy harvesting-storage bracelet incorporating electrochemical microsupercapacitors self-charged from a single hand gesture. *Adv. Energy Mater.* **2019**, *9*, 1900152.
(8) Pu, X.; Guo, H.; Chen, J.; Wang, X.; Xi, Y.; Hu, C.; Wang, Z. Eye motion triggered self-powered mechnosensational communication system using triboelectric nanogenerator. *Sci. Adv.* **2017**, *3*, 1700694.
(9) Yang, P.; Liu, K.; Chen, Q.; Mo, X.; Zhou, Y.; Li, S.; Feng, G.; Zhou, J. Wearable thermocells based on gel electrolytes for the utilization of body heat. *Angew. Chem., Int. Ed.* **2016**, *55*, 12050−12053.
(10) Chen, T.; Qiu, L.; Yang, Z.; Cai, Z.; Ren, J.; Li, H.; Lin, H.; Sun, X.; Peng, H. An integrated "energy wire" for both photoelectric conversion and energy storage. *Angew. Chem., Int. Ed.* **2012**, *51*, 11977−11980.
(11) Huang, X.; Han, S.; Huang, W.; Liu, X. Enhancing solar cell efficiency: the search for luminescent materials as spectral converters. *Chem. Soc. Rev.* **2013**, *42*, 173−201.
(12) Hao, S.; Shang, Y.; Li, D.; Ågren, H.; Yang, C.; Chen, G. Enhancing dye-sensitized solar cell efficiency through broadband near-infrared upconverting nanoparticles. *Nanoscale* **2017**, *9*, 6711−6715.
(13) Shao, Y.; El-Kady, M. F.; Sun, J.; Li, Y.; Zhang, Q.; Zhu, M.; Wang, H.; Dunn, B.; Kaner, R. B. Design and mechanisms of asymmetric supercapacitors. *Chem. Rev.* **2018**, *118*, 9233−9280.
(14) Lin, Y.; Gao, Y.; Fan, Z. Printable fabrication of nanocoral-structured electrodes for high-performance flexible and planar supercapacitor with artistic design. *Adv. Mater.* **2017**, *29*, 1701736.
(15) Jin, M.; Zhang, Y.; Yan, C.; Fu, Y.; Guo, Y.; Ma, X. High-performance ionic liquid-based gel polymer electrolyte incorporating anion-trapping boron sites for all-solid-state supercapacitor application. *ACS Appl. Mater. Interfaces* **2018**, *10*, 39570−39580.
(16) Liu, N.; Gao, Y. Recent progress in micro-supercapacitors with in-plane interdigital electrode architecture. *Small* **2017**, *13*, 1701989.
(17) Guo, R.; Chen, J.; Yang, B.; Liu, L.; Su, L.; Shen, B.; Yan, X. In-plane micro-supercapacitors for an integrated device on one piece of paper. *Adv. Funct. Mater.* **2017**, *27*, 1702394.
(18) Li, Z.; Cao, L.; Qin, P.; Liu, X.; Chen, Z.; Wang, L.; Pan, D.; Wu, M. Nitrogen and oxygen co-doped graphene quantum dots with high capacitance performance for micro-supercapacitors. *Carbon* **2018**, *139*, 67−75.
(19) Zhu, M.; Huang, Y.; Huang, Y.; Li, H.; Wang, Z.; Pei, Z.; Xue, Q.; Geng, H.; Zhi, C. A highly durable, transferable, and substrate-versatile high-performance all-polymer micro-supercapacitor with plug-and-play function. *Adv. Mater.* **2017**, *29*, 1605137.
(20) Li, Z.; Ma, G.; Ge, R.; Qin, F.; Dong, X.; Meng, W.; Liu, T.; Tong, J.; Jiang, F.; Zhou, Y.; Li, K.; Min, X.; Huo, K.; Zhou, Y. Free-standing conducting polymer films for high-performance energy devices. *Angew. Chem., Int. Ed.* **2016**, *55*, 979−982.
(21) Boles, M. A.; Engel, M.; Talapin, D. V. Self-assembly of colloidal nanocrystals: from intricate structures to functional materials. *Chem. Rev.* **2016**, *116*, 11220−11289.
(22) Oszajca, M. F.; Bodnarchuk, M. I.; Kovalenko, M. V. Precisely engineered colloidal nanoparticles and nanocrystals for Li-ion and Na-ion batteries: model systems or practical solutions? *Chem. Mater.* **2014**, *26*, 5422−5432.
(23) Jiao, Y.; Han, D.; Ding, Y.; Zhang, X.; Guo, G.; Hu, J.; Yang, D.; Dong, A. Fabrication of three-dimensionally interconnected nanoparticle superlattices and their lithium-ion storage properties. *Nat. Commun.* **2015**, *6*, 6420.
(24) Wu, W.; Wang, L.; Yuan, J.; Zhang, Z.; Zhang, X.; Dong, S.; Hao, J. Formation and degradation tracking of a composite hydrogel based on UCNPs@PDA. *Macromolecules* **2020**, *53*, 2430−2440.
(25) Wu, W.; Liu, H.; Yuan, J.; Zhang, Z.; Wang, L.; Dong, S.; Hao, J. Nanoemulsion fluorescent inks for anti-counterfeiting encryption with dual-mode, full-color, and long-term stability. *Chem. Commun.* **2021**, *57*, 4894−4897.
(26) Wu, W.; Wang, L.; Wang, Y.; Guo, L.; Dong, S.; Hao, J. Colloidal clusters of icosahedrons and face-centred cubes. *J. Colloid Interface Sci.* **2020**, *563*, 308−317.
(27) Bai, F.; Wang, D.; Huo, Z.; Chen, W.; Liu, L.; Liang, X.; Chen, C.; Wang, X.; Peng, Q.; Li, Y. A versatile bottom-up assembly approach to colloidal spheres from nanocrystals. *Angew. Chem., Int. Ed.* **2007**, *46*, 6650−6653.
(28) Zhang, X.; Lin, M.; Lin, X.; Zhang, C.; Wei, H.; Zhang, H.; Yang, B. Plypyrrole-enveloped Pd and Fe_3O_4 nanoparticle binary hollow and bowl-like superstructures as recyclable catalysts for industrial wastewater treatment. *ACS Appl. Mater. Interfaces* **2014**, *6*, 450−458.
(29) Park, J.; Hickey, D. R.; Jun, S.; Kang, S.; Hu, X.; Chen, X. J.; Park, S. J. Surfactant-assisted emulsion self-assembly of nanoparticles into hollow vesicle-like structures and 2D plates. *Adv. Funct. Mater.* **2016**, *26*, 7791−7798.
(30) Li, R. Z.; Peng, R.; Kihm, K. D.; Bai, S.; Bridges, D.; Tumuluri, U.; Wu, Z.; Zhang, T.; Compagnini, G.; Feng, Z.; Hu, A. High-rate in-plane micro-supercapacitors scribed onto photo paper using in situ femtolaser-reduced graphene oxide/Au nanoparticle microelectrodes. *Energy Environ. Sci.* **2016**, *9*, 1458−1467.
(31) Wang, S.; Yu, Y.; Li, R.; Feng, G.; Wu, Z.; Compagnini, G.; Gulino, A.; Feng, Z.; Hu, A. High-performance stacked in-plane supercapacitors and supercapacitor array fabricated by femtosecond laser 3D direct writing on polyimide sheets. *Electrochim. Acta* **2017**, *241*, 153−161.
(32) Zhang, C.; McKeon, L.; Kremer, M. P.; Park, S. H.; Ronan, O.; Seral-Ascaso, A.; Barwich, S.; Coileáin, C. Ó; McEvoy, N.; Nerl, H. C.; Anasori, B.; Coleman, J. N.; Gogotsi, Y.; Nicolosi, V. Additive-free MXene inks and direct printing of micro-supercapacitors. *Nat. Commun.* **2019**, *10*, 1−9.
(33) Liu, W.; Feng, Y. Q.; Yan, X. B.; Chen, J. T.; Xue, Q. J. Superior micro-supercapacitors based on graphene quantum dots. *Adv. Funct. Mater.* **2013**, *23*, 4111−4122.
(34) Auzel, F. Upconversion and anti-stokes processes with f and d ions in solids. *Chem. Rev.* **2004**, *104*, 139−173.

(35) Zhang, Y.; Huang, L.; Liu, X. Unraveling epitaxial habits in the $NaLnF_4$ system for color multiplexing at the single-particle level. *Angew. Chem., Int. Ed.* **2016**, *55*, 5718−5722.
(36) Gnanasammandhan, M. K.; Idris, N. M.; Bansal, A.; Huang, K.; Zhang, Y. Near-IR photoactivation using mesoporous silica-coated $NaYF_4$:Yb,Er/Tm upconversion nanoparticles. *Nat. Protoc.* **2016**, *11*, 688−713.
(37) Yang, B.; Wang, Y.; Wei, T.; Pan, Y.; Zhou, E.; Yuan, Z.; Han, Y.; Li, M.; Ling, X.; Yin, L.; Xie, X.; Huang, L. Solution-processable near-infrared-responsive composite of perovskite nanowires and photon-upconversion nanoparticles. *Adv. Funct. Mater.* **2018**, *28*, 1801782.

https://doi.org/10.1021/acscentsci.1c00795
ACS Cent. Sci. 2021, 7, 1611−1621